Analysis of Power Flow by Poynting Vectors for Electromagnetic Wave Absorbers Using Frequency Selective Surfaces

Takahiko Yoshida[1, *], Masato Matsushita[2], Takumi Kubota[1], and ShinzoYoshikado[1]

Abstract—The power flow for electromagnetic wave absorbers consisting of pattern conductor layers acting as frequency selective surfaces, absorption layers, and short circuit layers was investigated by Poynting vectors. A method was developed to evaluate the flow of electromagnetic wave power by an electromagnetic wave absorber upon irradiation with electromagnetic waves. The results indicate that the electromagnetic wave absorption phenomenon involves generation of real power, a real part of the time averaged Poynting vector, which moves horizontally along the pattern surface after the incident wave has irradiated the pattern conductor from the vertical direction, and the direction of power flow changes to enter the polymer layer from the pattern interval, causing an accumulation of power inside the polymer layer, followed by absorption, which is converted into heat due to the loss factor.

1. INTRODUCTION

Electromagnetic wave absorbers (referred to hereafter simply as absorbers) are devices that convert the energy of incident electromagnetic radiation into heat *via* conductive, dielectric, and/or magnetic losses [1–6]. For example, absorbers made of magnetic materials, such as ferrite ceramics or rubber ferrites (in which ferrite powders are incorporated into a polymer), exhibit wideband frequency absorption characteristics upon magnetic loss, and have been used in practical applications up to frequencies of several GHz. Previous reports have indicated that the use of carbonyl iron particles and/or sendust alloys in an absorber increases its thermal conductivity,thereby avoiding overheating of devices. However, devices using such absorbers are quite heavy due to the incorporation of as much as 85–95 wt% of magnetic metal powder, and can be costly [1–3].

Several design factors for absorbers must be considered. Maximum absorption is obtained when the input impedance at the incident surface of the absorber is the same as the characteristic impedance of free space, a situation referred to as the non-reflective condition. In addition, when fabricating an absorber made of a homogeneous material, the key parameters are the thickness of the device and the complex relative permittivity and complex relative permeability of the material. However, even if the permittivity and permeability are optimal, reducing the thickness of a homogeneous absorber can be difficult.

To overcome these challenges, absorbers whose performance can be tuned by varying their structural factors have been proposed, including the pattern arranged conductor backed absorber [7]. The present study describes the investigation of a conductor backed absorber that incorporates a patterned layer composed of periodically arranged multiple pattern conductors (referred to as pattern conductors) on the incident side, referred to as a pattern absorber. A study of the design and evaluation of pattern absorbers has been reported [8]. The pattern absorber stores a portion of the electromagnetic power from the incident electromagnetic waves and subsequently converts this energy into heat *via* a quality factor (Q value) of resonator, which consists of a patterned layer, an absorption layer with a dielectric

and/or magnetic loss, and a back reflector. The resonant frequency is determined not by the thickness of the absorption layer but by each size of each component. Waves that are not absorbed are re-radiated out of the absorber. Absorption results from the interference of waves reflected by the absorber and the absorbed power is subsequently converted into heat. The structure of this device is expected to allow the development of thinner pattern absorbers, because the thickness of the pattern absorber is determined by the size of the pattern conductor, whereas the thickness of the absorption layer (such as the dielectric layer and/or the magnetic layer) has no significant effect, in contrast to the $\lambda/4$ type absorber [8, 9].

Generally, an FSS (frequency selective surface) is used for antennae and electromagnetic wave shielding films. A patterned layer with an FSS (an FSS patterned layer) has been reported as an impedance design factor that allows the fabrication of a thinner absorber [9]. However, the reports of absorbers using FSS patterned layers do not provide details about the pattern shape, arrangement, and power flows related to electromagnetic wave absorption through which the optimum electromagnetic wave absorption is achieved.

The least understood feature of absorbers is the disappearance of electromagnetic energy through the interference between the incident wave and reflected wave, which ignores the law of energy conservation. It is particularly difficult to explain the reason by which the power of the electromagnetic wave disappears when it is reflected directly from a pattern conductor placed on the surface of a pattern absorber. The present study clarifies the power flow of the electromagnetic wave reflected directly from a pattern conductor of an electromagnetic wave absorber having an FSS patterned layer using the time averaged Poynting vector representing the flow of the electromagnetic wave power [10–12].

2. EXPERIMENTAL PRINCIPLE AND EXPERIMENTS

2.1. Poynting Vector

To evaluate the flow of power generated by an electromagnetic wave absorber, the time averaged complex Poynting vector $\vec{S}$ [J/m^2·s] (hereafter, Poynting vector) was calculated with an electric field $\vec{E}$ and magnetic field $\vec{H}$ at each point on/above and in the electromagnetic wave absorber, according to the equation:

$$\vec{S} = \vec{E} \times \vec{H}^* = (E_y H_z^* - E_z H_y^*, E_z H_x^* - E_x H_z^*, E_x H_y^* - E_y H_x^*) \equiv (S_x, S_y, S_z) \tag{1}$$

Here, E_x, E_y, and E_z are the x, y and z components, respectively, of $\vec{E}$ at each point, and H_x, H_y and H_z are the x, y and z components of $\vec{H}$ at each point. The symbols $\vec{H}^*$ and H_x^* denote the complex conjugates of $\vec{H}$ and H_x, respectively [10–12]. The strength of each component, in consideration of the anisotropy of the absorber, is expressed by:

$$
\begin{aligned}
E_x &= |E_x|\, e^{j(\omega t + \alpha_x)} \equiv E_{xr} + jE_{xi}, \ H_x = |H_x|\, e^{j(\omega t + \beta_x)} \equiv H_{xr} + jH_{xi}, \\
E_y &= |E_y|\, e^{j(\omega t + \alpha_y)} \equiv E_{yr} + jE_{yi}, \ H_y = |H_y|\, e^{j(\omega t + \beta_y)} \equiv H_{yr} + jH_{yi}, \\
E_z &= |E_z|\, e^{j(\omega t + \alpha_z)} \equiv E_{zr} + jE_{zi}, \ H_z = |H_z|\, e^{j(\omega t + \beta_z)} \equiv H_{zr} + jH_{zi}
\end{aligned}
\tag{2}
$$

In these equations, j is the imaginary unit, ω [rad] the angular velocity, and t [s] time. Also, $\vec{E}$ and $\vec{H}$ have a phase angle taking anisotropy into consideration. The α_x, α_y, and α_z terms indicate the phase angles of $\vec{E}$ and β_x, β_y and β_z terms indicate the phase angles of $\vec{H}$ at each point (x, y, z). The terms E_x, E_y, E_z, H_x, H_y, and H_z are complex numbers, with real parts E_{xr}, E_{yr}, E_{zr}, H_{xr}, H_{yr}, and H_{zr}, respectively, and imaginary parts E_{xi}, E_{yi}, E_{zi}, H_{xi}, H_{yi}, and H_{zi}. The S_x, S_y, and S_z terms are expressed by the following:

$$
\begin{aligned}
S_x &= [(E_{yr} + jE_{yi})(H_{zr} - jH_{zi}) - (E_{zr} + jE_{zi})(H_{yr} - jH_{yi})] \equiv S_{xr} + jS_{xi} \\
S_y &= [(E_{zr} + jE_{zi})(H_{xr} - jH_{xi}) - (E_{xr} + jE_{xi})(H_{zr} - jH_{zi})] \equiv S_{yr} + jS_{yi} \\
S_z &= [(E_{xr} + jE_{xi})(H_{yr} - jH_{yi}) - (E_{yr} + jE_{yi})(H_{xr} - jH_{xi})] \equiv S_{zr} + jS_{zi}
\end{aligned}
\tag{3}
$$

S_{xr}, S_{yr}, and S_{zr} are the real parts, and S_{xi}, S_{yi}, and S_{zi} are the imaginary parts of S_x, S_y, and S_z, respectively. The time averaged power dP transmitted across a differential area ds is given by:

$$dP = \frac{1}{2}\text{Re}\left(\vec{S}\right) \cdot d\vec{s} = \text{Re}\left[\frac{1}{2}\left(\vec{E} \times \vec{H}^*\right)\right] \cdot d\vec{s} \tag{4}$$

where Re indicates the real part of the complex number, and $d\vec{s}$ is the differential area vector of ds. Conventionally, the imaginary part of $\vec{S}$ is seldom discussed. The sign of the real and imaginary parts of each component of $\vec{S}$ is positive for the positive direction and negative for the negative direction of the defined orthogonal xyz coordinate system.

Using the phase angle difference, the Poynting vector can be represented by:

$$\begin{aligned}
S_x &= \left[|E_y|\,|H_z|\,e^{j(\alpha_y-\beta_z)} - |E_z|\,|H_y|\,e^{j(\alpha_z-\beta_y)}\right] \\
S_y &= \left[|E_z|\,|H_x|\,e^{j(\alpha_z-\beta_x)} - |E_x|\,|H_z|\,e^{j(\alpha_x-\beta_z)}\right] \\
S_z &= \left[|E_x|\,|H_y|\,e^{j(\alpha_x-\beta_y)} - |E_y|\,|H_x|\,e^{j(\alpha_y-\beta_x)}\right]
\end{aligned} \tag{5}$$

Attenuation or power loss is included in the absolute value of each component. To compare the magnitudes of the components of the Poynting vector, S_{xr0}, S_{yr0}, S_{zr0}, S_{xi0}, S_{yi0}, and S_{zi0} were used and normalized by dividing each value of the real and imaginary parts of each component by the absolute value of the Poynting vector of the incident wave (only z component). Hereafter, normalized Poynting vectors $\vec{S}_0$ are used.

2.2. Simulation Experiments

The return loss R_L for the designed pattern absorber was calculated using:

$$R_L = 20\log_{10}|\Gamma_d| \tag{6}$$

where Γ_d is the complex voltage reflection coefficient given by:

$$\dot{\Gamma}_d = \frac{Z_s/Z_0 - 1}{Z_s/Z_0 + 1} \equiv \frac{z_s - 1}{z_s + 1} \tag{7}$$

in which Z_0 is the characteristic impedance of free space ($\sqrt{\mu_0/\varepsilon_0} \approx 376.73431\,\Omega$, μ_0 and ε_0 are the permeability and permittivity of free space, respectively; hereafter, $377\,\Omega$); Z_s is the input impedance at the absorber surface; $z_s(= Z_s/Z_0)$ is the normalized input impedance. The non-reflective condition for the absorber is $z_s = 1 + j0$.

The structure of the designed pattern absorber is shown in Fig. 1 [8]. A layer of aluminum foil layer approximately $9.5\,\mu\text{m}$ thick is attached to a polyethylene terephthalate (PET) film, serving as both the patterned layer and back reflector of the absorber, which is applied to the absorption layer (referred to as the polymer layer). The pattern conductor was generated by etching. In the pattern absorber, the polymer layer, made of dielectric and/or magnetic material, is used to support the patterned layer, construct the resonator with pattern conductor and back reflector, and convert the energy of electromagnetic waves into heat. The detail of fabrication of the polymer layer is shown in [8].

A $0.5\,\text{mm}$ thick magnetic layer was applied on the incident side, and a $2.0\,\text{mm}$ thick dielectric layer was applied on the back reflector side to represent the polymer layer. The total thickness d_{tot} of the polymer layer was $2.5\,\text{mm}$, so that $d_{\text{tot}}/\lambda_0 \ll 0.025$ (where λ_0 is the wavelength corresponding to the absorption center frequency f_0). The values of μ_r^* and ε_r^* measured at $2.45\,\text{GHz}$ for ML_1 (the magnetic layer) and DL_1 (the dielectric layer) are shown in Table 1, for materials fabricated practically [8].

In the simulation, the aluminum conductivity value was set to $3.54 \times 10^7\,\text{S/m}$. Tests confirmed that the electromagnetic wave shielding properties of this conductor were sufficient for the calculations. The effects of the PET film and adhesive used for lamination were negligible in the simulation. Simulation of the absorption characteristics was performed on a square pattern conductor with side length L determined to be $21\,\text{mm}$ from f_0, as shown in Fig. 2(a), with the material constants of the polymer
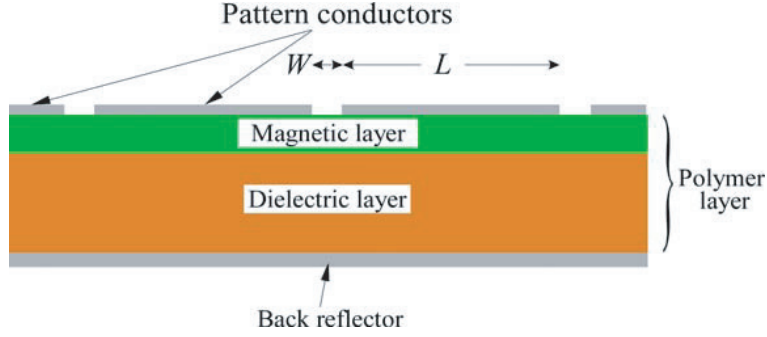
Figure 1. Structure of the pattern absorber.

layer as shown in Table 1. It was confirmed that the simulated results of absorbing characteristics agreed with the measured values [8]. W is the interval (hereafter, the pattern interval) between the ends of adjacent patterns (hereafter, the pattern edges). The area enclosed by the dashed lines in Fig. 2(a) represents the unit cell. Since the pattern absorber consists of a periodic arrangement of unit cells, both the electric walls and magnetic walls of the simulation were placed perpendicular to the electric and magnetic field of plane waves, respectively, at the boundaries of the unit cells to create a periodic boundary condition, shown as the periodic structure in Fig. 2(b), when determining the electromagnetic field distribution [13]. The orthogonal xyz coordinate system is defined as shown in Figs. 2(a) and (b). An electromagnetic power source located 300 mm in the z-axis direction from the surface of the absorber (to ensure a uniform electromagnetic field) was used to generate plane waves incident at a right angle to the unit cell. A plane wave with an electric field component parallel to the y-axis was incident on the pattern conductor.

Table 1. Material constants for each layer at 2.45 GHz.

Layer	Designation	μ_r'	μ_r''	ε_r'	ε_r''
Magnetic layer	ML_1	1.37	0.51	13.56	1.25
Dielectric layer	DL_1	1.00	0	3.50	0

The black spots shown in the unit cell in Fig. 2(a) are analysis points (x, y, z) for the pattern absorber, where x and y are fixed and z moves in the range between -2.5 and 300 mm. The range between -2.5 mm and 0 corresponds to the polymer layer and that between 0 and 300 mm corresponds to the sky as shown in Fig. 2(b). The position $z = 0$ is the pattern conductor or the upper end position of the polymer layer. An incident plane wave having a magnetic field component H_x parallel to the x-axis and electric field component E_y parallel to the y-axis oscillates from the port (feeding point) of the upper part in the z-axis direction of the incident wave [see Fig. 2(b)]. The reflection characteristics were evaluated using the transmission line matrix (TLM) method [13]. The electromagnetic field distribution was obtained using a simulator (MWSTUDIO, Computer Simulation Technology AG) based on FD-TD. In this study, the vertical incidence of electromagnetic waves is treated [14–16].

3. RESULTS AND DISCUSSION

3.1. Validity of the Analysis by Poynting Vector

To evaluate the validity of the analysis by Poynting vector, a unit cell was constructed as a uniform surface instead of a pattern diagram, and as a perfect reflecting surface with a resistance value of $0\,\Omega$ corresponding to $W = 0$, and a fully absorbing surface equivalent to $377\,\Omega$. Figs. 3 and 4 show normalized Poynting vectors $\vec{S}_0$ and phase angle differences, e.g., $\alpha_y - \beta_x$, for a perfect reflecting surface and a fully absorbing surface, respectively, on the unit cell at $z = 0$ and every 5 mm from 0 to 300 mm in the z-axis direction when electromagnetic waves are incident. The analysis results are shown for
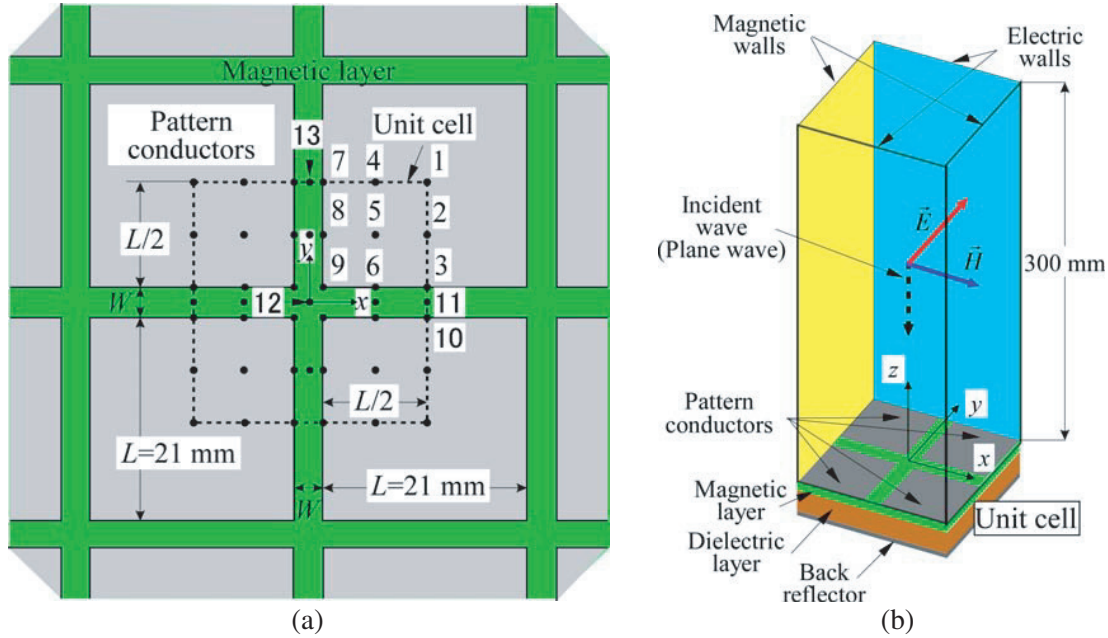
Figure 2. Pattern shape, unit cell, analysis points, and periodic structure in the pattern absorbers. (a) Pattern shape and analysis points. (b) Simulation domain (unit cell).
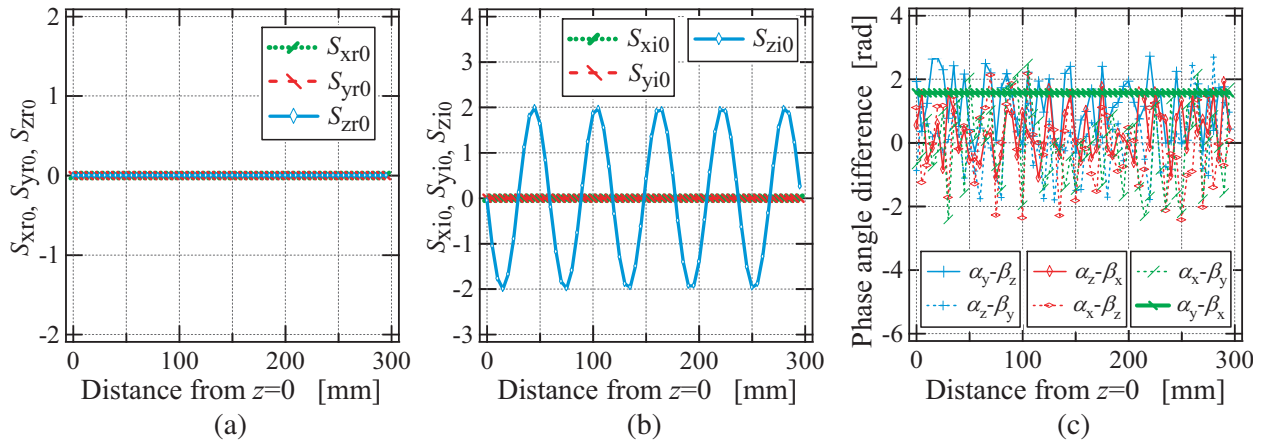

Figure 3. Normalized Poynting vectors and phase angle differences for a perfect reflecting surface. (a) Real parts of normalized Poynting vector, (b) imaginary parts of normalized Poynting vector, (c) phase angle differences, e.g., $\alpha_y - \beta_x$.

the steady state after incidence and reflection are repeated. On the perfect reflecting surface, both the real and imaginary parts of the x and y components of $\vec{S}_0$ were zero, and S_{zr0} in the sky did not depend on the distance from the absorber in the z-axis direction and became 0, as shown in Fig. 3(a), because the Poynting vector of the incident wave and the Poynting vector of the reflected wave have the same absolute values and the signs were opposite, indicating that power was not input to the net absorber. In contrast, S_{zi0} was not 0 and oscillated with a wavelength of one-half of the spatial wavelength. The behavior of S_{zi0} indicated a power standing wave with twice the amplitude of the incident wave intensity (Fig. 3(b)). This is similar to the standing wave of the electric field, indicating that the imaginary part of the Poynting vector interfered in the same way as the electric and magnetic fields. S_{zi0} indicates reactive power flow and the space averaged value is 0. As shown in Fig. 3(c), only
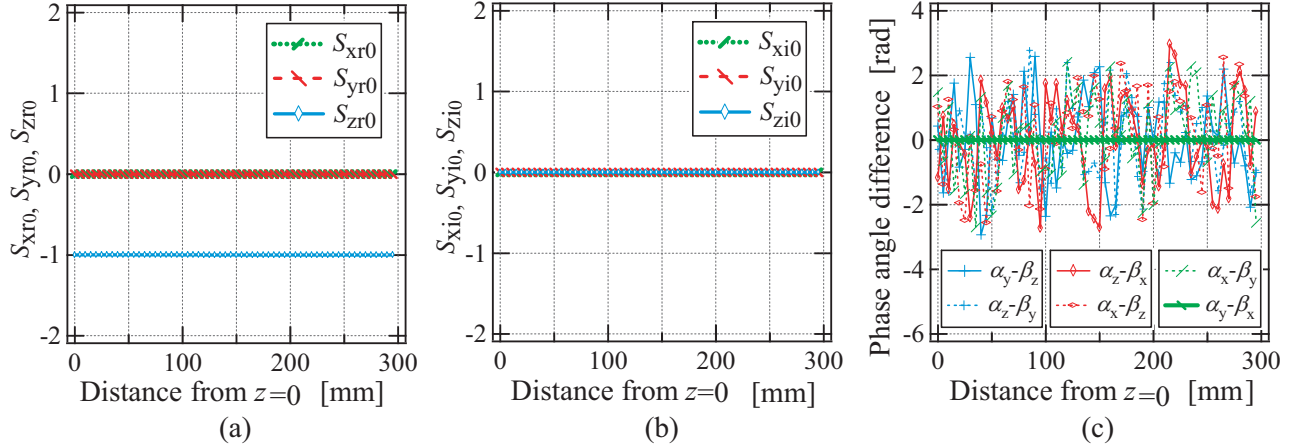
Figure 4. Normalized Poynting vectors and phase angle differences for a fully absorbing surface. (a) Real parts of normalized Poynting vector, (b) imaginary parts of normalized Poynting vector, (c) phase angle differences, e.g., $\alpha_y - \beta_x$.

the phase angle difference $\alpha_y - \beta_x$ corresponding to S_z in Eq. (5) does not depend on distance and possesses a constant value of $\pi/2$ rad in the case of a perfect reflecting surface.This corresponds well to the difference between the phase angles of the standing waves of the electric field and magnetic field in the case of perfect reflection. The phase angle differences other than $\alpha_y - \beta_x$ varied widely because the uncertainty of the phase angle difference increases due to the extremely small magnitude of the electric and magnetic fields. In addition, S_{xr0}, S_{xi0}, S_{yr0}, and S_{yi0} were all 0, indicating no power flow occurred in any direction other than the z-axis direction. When incident on a fully absorbing surface, S_{zr0} does not depend on distance and becomes -1 (S_{zi0} is 0), indicating no reflected wave, as shown in Figs. 4(a) and (b). Since the other components are 0, no power flow occurred in any direction other than the z-axis direction. As shown in Fig. 4(c), the difference between the phase angles was also 0 only for $\alpha_y - \beta_x$.

3.2. Absorption Characteristics and Poynting Vector for the Pattern Absorbers

The absorption properties were simulated using the square pattern shown in Fig. 2(a). The value of z_s was estimated from the electromagnetic field at the source position. The absorption characteristics of these devices are summarized in Table 2, showing z_{sr} as the real part of z_s, z_{si} as the imaginary part of z_s, $\Delta f / f_0$ as the -20 dB absorption frequency bandwidth, and Δf as the frequency range over which

Table 2. Pattern parameters and absorbing characteristics for pattern absorbers.

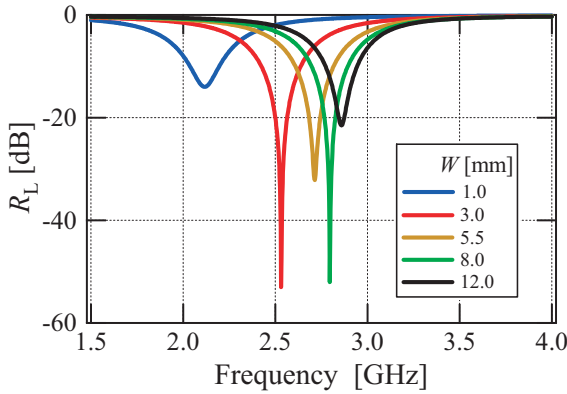| Pattern interval W [mm]	1.0	3.0	5.5	8.0	12.0
Pattern area ratio P	0.911	0.766	0.628	0.524	0.405
f_0 [GHz]	2.117	2.532	2.714	2.796	2.860
R_L [dB]	-14.02	-53.02	-32.17	-52.06	-21.53
Γ_{dr}	-0.199	-0.000	0.025	-0.003	-0.084
Γ_{di}	-0.011	0.002	-0.001	0.015	0.005
z_{sr}	0.668	0.999	1.052	0.995	0.846
z_{si}	-0.016	0.004	-0.001	0.002	0.009
-20 dB bandwidth ($\Delta f / f_0$)	0	0.0271	0.0241	0.0226	0.0125
d_{tot}/λ_0	0.0177	0.0211	0.0226	0.0233	0.0238

Figure 5. Frequency dependence of R_L for pattern absorbers.
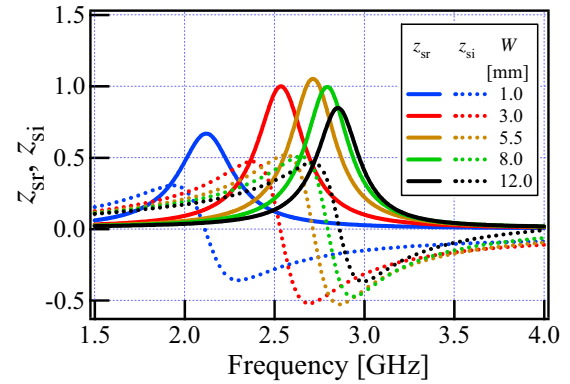

Figure 6. Frequency dependencies of z_{sr} and z_{si} for pattern absorbers.

the return loss R_L is less than -20 dB. P is the occupied area ratio of the pattern conductor to total area of the unit cell. The frequency dependence of R_L is shown in Fig. 5, while variations in z_{sr} and z_{si} with frequency are presented in Fig. 6. The value of z_{sr} reached a maximum when z_{si} was nearly zero at f_0. The frequency dependence is similar to the typical parallel resonator. When $z_s = 1 + j0$, the minimum R_L value was obtained and absorption was maximized, as shown in Figs. 5 and 6. This is a matching state. When W increases, f_0 tends to shift toward the lower frequencies beyond the resonance frequency defined by the pattern dimension (Table 2). When W increased at f_0, z_{sr} increased and then decreased after showing a maximum as shown in Fig. 6 [8]. In this pattern absorber, the maximum value of z_s was equal to $1 + j0$ for $W = 3$ and 8 mm. Normalized Poynting vectors were calculated in a fixed point (position 1 shown in Fig. 2(a)) for the positive side in the z-axis positive direction (in free space) every 5 mm for $z = 0$ to 300 mm shown in Fig. 2(b), and for $W = 1$, 3, 8, and 12 mm (Figs. 7(a)–(h)). At $z = 0$ mm, $S_{zr0} = 0$ because it is directly incident on the pattern conductor and the electric field strength is 0 on the surface of the conductor, but S_{zr0} becomes nearly constant in the sky above $z \approx +25$ mm, regardless of the matching state from each W. This value was nearly -1 for $W = 3$ and 8 mm as a matching state (near non-reflective condition) as shown in Figs. 7(b) and (c). On the other hand, the matching state is not reached for $W = 1$ and 12 mm as shown in Figs. 7(a) and (d), because S_{zr0} did not become -1 and S_{zi0} showed oscillatory behavior. The amplitude intensity of S_{zi0} was inversely proportional to the matching state, and was correlated with R_L. Fig. 7(i) shows the phase angle difference $\alpha_y - \beta_x$ of the reflected wave at each value of W with respect to the incident wave. $\alpha_y - \beta_x$ also exhibited oscillatory behavior depending on the matching state. When a matching state was reached, $\alpha_y - \beta_x$ was nearly constant at 0, regardless of the position. Even when the conductor occupied area ratio became large $[W = 1 \text{ mm } (P = 0.911)]$, it approached the state of perfect reflection. However, $\alpha_y - \beta_x$ showed a marked oscillating behavior shown in Fig. 8(i) and was very different from the results shown in Fig. 3(c). This indicates that power flow occurred from the polymer layer through the pattern interval between the pattern conductors.

Next, with the matching condition of $W = 3$ mm, the normalized Poynting vector component was calculated in all black points shown in Fig. 2(a). Some of these real parts in the sky are shown in Fig. 8. When a plane wave with an electric field component parallel to the y-axis was incident on the pattern conductor, the pattern edge (side length) of the square pattern parallel to the y-axis became the resonance portion. S_{xr0} in all the positions was almost 0 except for in the vicinity of the pattern corner (position 9). S_{zr0} in all positions became -1 (the matching state) at $z \geq \sim 15$ mm in the sky. S_{zr0} was 0 on the pattern conductor except for the pattern edge parallel to the x-axis at $z = 0$ as shown in Fig. 8. S_{yr0} became stronger horizontally (at constant z) from position 1 (the center of the conductor) or 4 to the pattern edge (position 3 or 6, respectively) parallel to the x-axis near the pattern conductor ($0 \leq z \leq \sim 15$ mm), and exhibited behavior that was maximized at the pattern edge as shown in Figs. 8(a)–(h). On the other hand, S_{yr0} was almost constant horizontally from position 1 or 2 toward the pattern edge (position 7 or 8, respectively) parallel to the y-axis and changed rapidly near
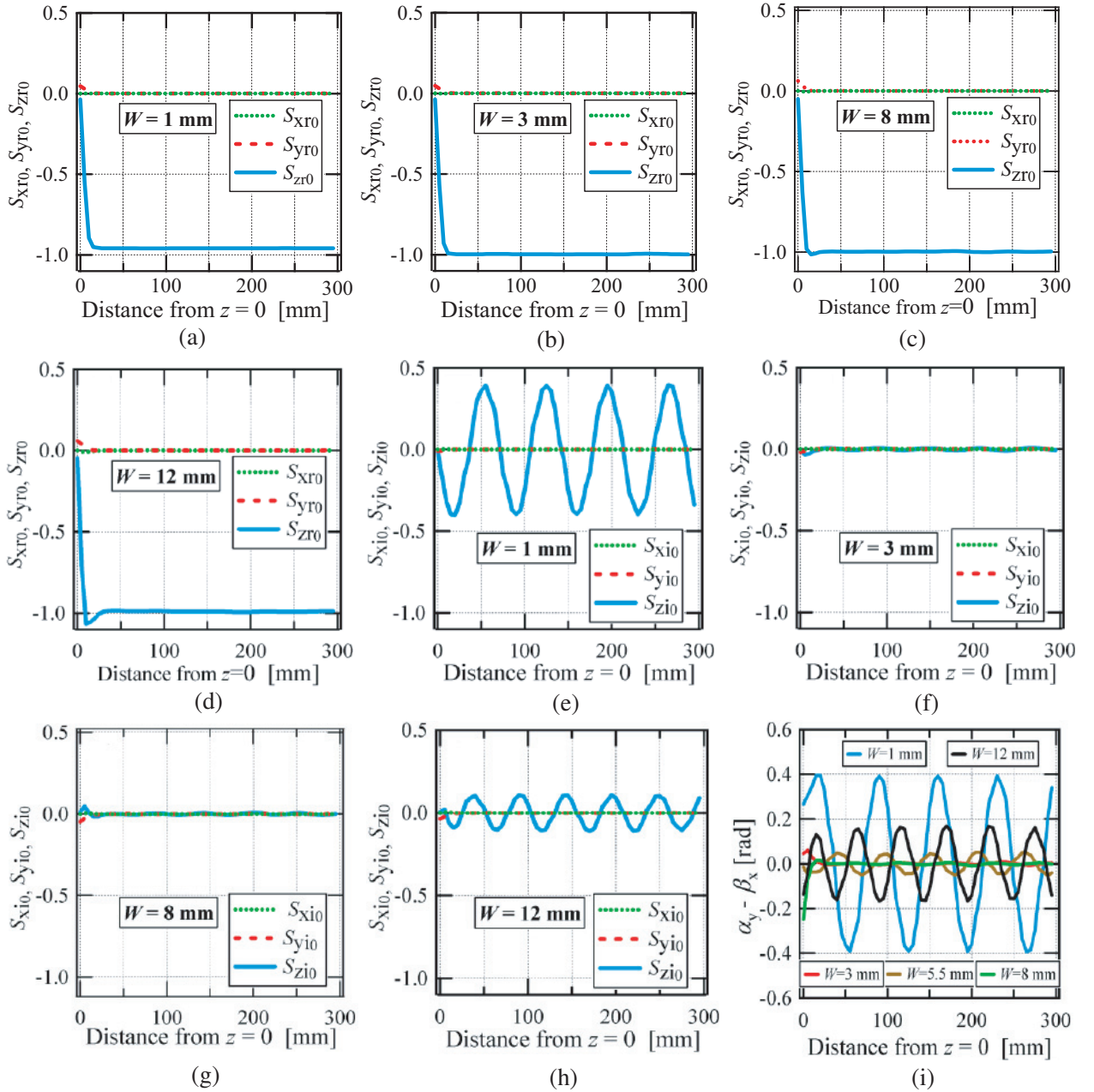
Figure 7. Normalized Poynting vectors and phase angle difference $\alpha_y - \beta_x$ for $W = 1$–12 mm in position 1 on the surface of the absorber and in the sky: (a)–(d) real parts, (e)–(h) imaginary parts, (i) $\alpha_y - \beta_x$.

the pattern edge. S_{yr0} in positions 3, 6, and 9 and at $z = 0$ was ~ 6–10-fold larger than the incident wave intensity as shown in Figs. 8(b), (e), and (h). In the positions 3 and 6, the real power flow S_{yr0} in the horizontal direction coming from the opposing pattern conductors joined the real power flows S_{zr0} coming down in the vertical direction into the pattern interval, and then they flowed into the polymer layer between the pattern conductor and the back reflector. The direction of S_{yr0} and S_{zr0} in the positions 3 and 10, which were located on the opposite side of position 3 through the pattern interval, was mutually opposite as shown in Figs. 8(b) and (i). As shown in Figs. 8(j) and (k), S_{xr0} in both the positions 11 and 12, which were located at the center of the pattern interval parallel to x axis, was almost 0. Therefore, power also flows in the direction parallel to the y-axis on the pattern conductor. S_{yr0} in both positions 11 and 12 was not zero and the sign was positive. However, the primary differential
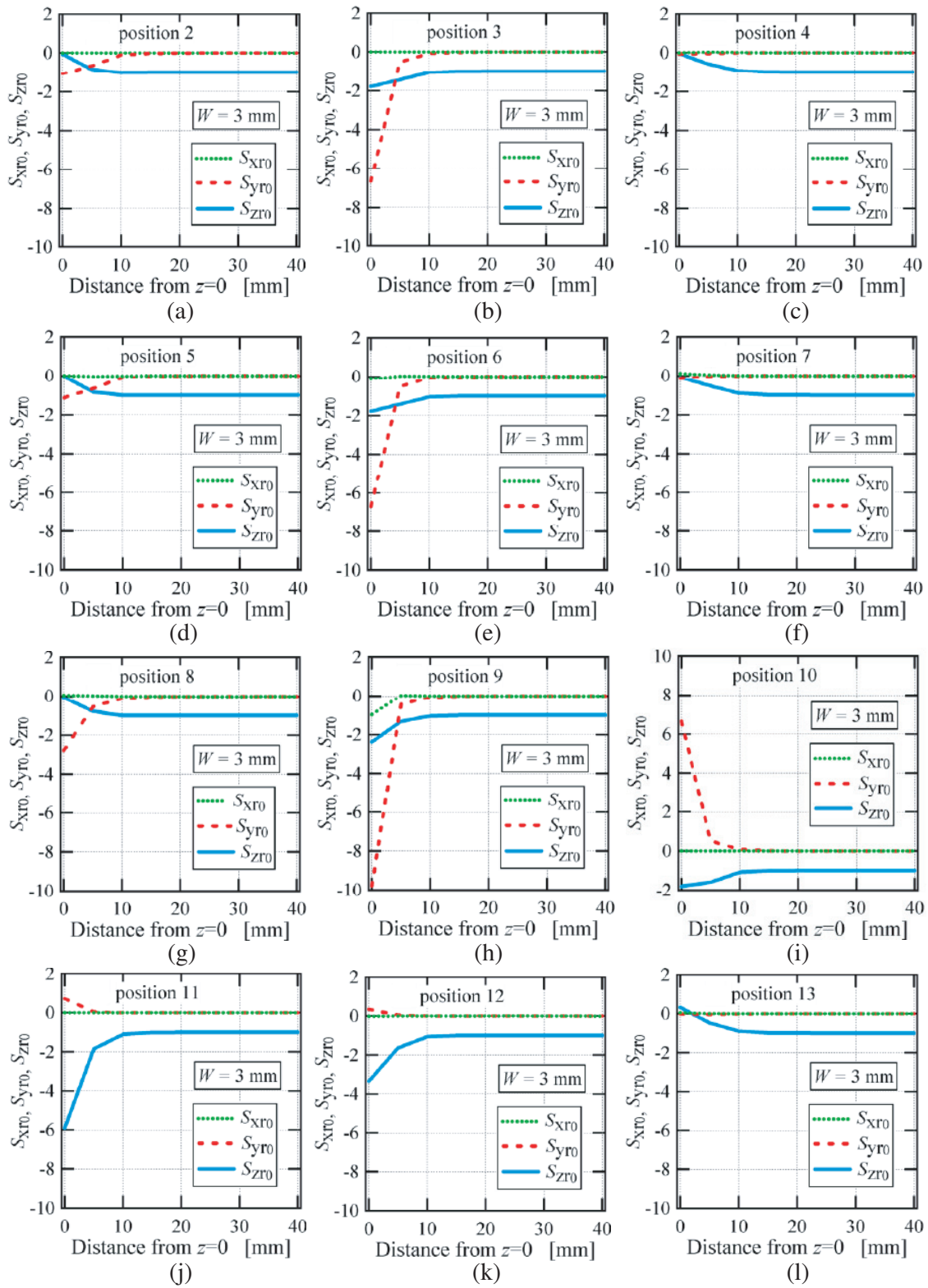
Figure 8. Real parts of normalized Poynting vectors for $W = 3\,\text{mm}$ in the positions (a) 2, (b) 3, (c) 4, (d) 5, (e) 6, (f) 7, (g) 8, (h)9, (i) 10, (j) 11, (k) 12, and (l) 13 on the surface of the absorber and in the sky.
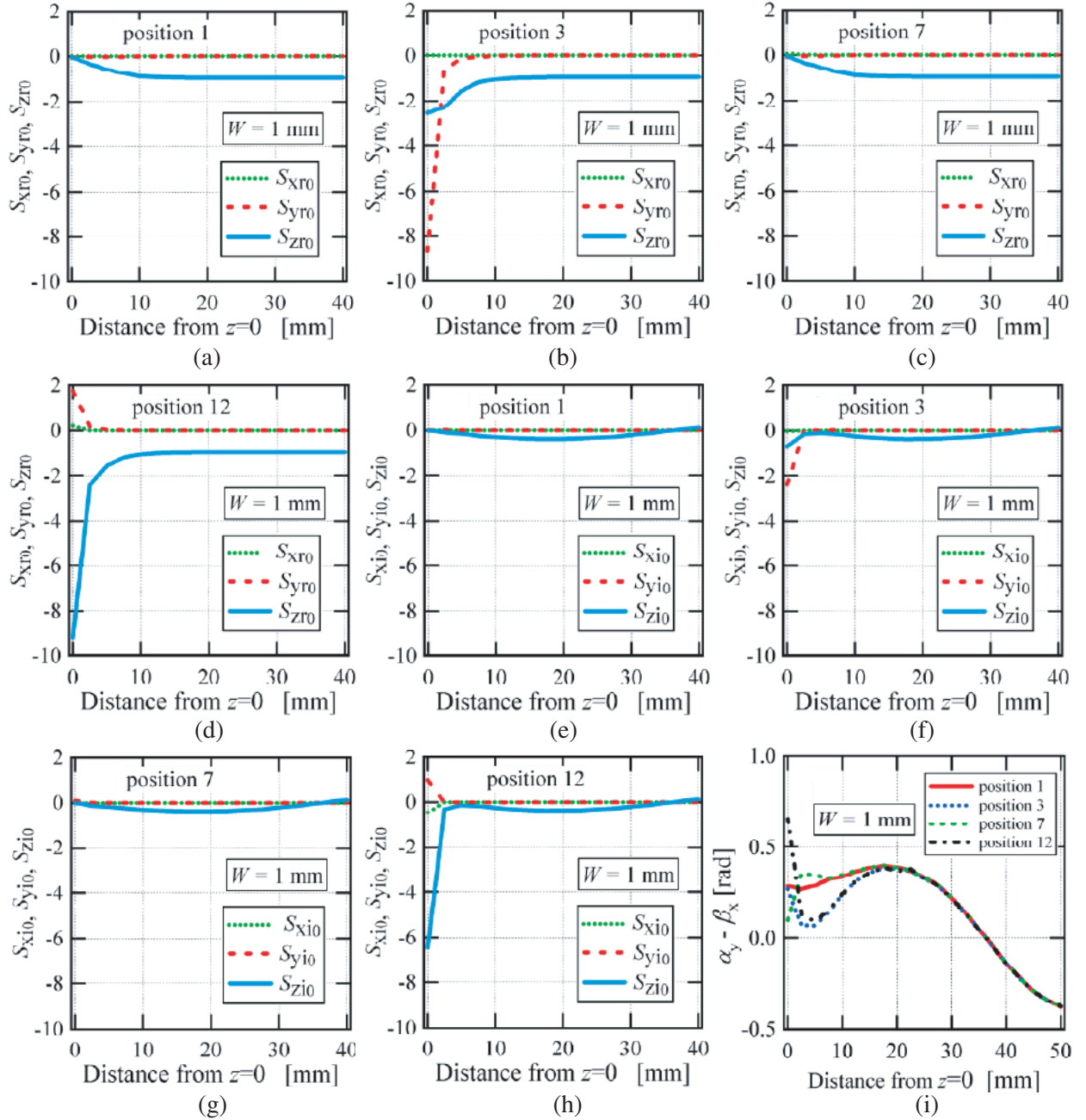
Figure 9. Real parts of normalized Poynting vectors for $W = 1$ mm in the positions (a) 1, (b) 3, (c) 7, (d) 12, and imaginary parts of normalized Poynting vectors in the positions (e) 1, (f) 3, (g) 7, (h) 12 and (i) phase angle difference $\alpha_y - \beta_x$ for each position on the surface of the absorber and in the sky.

coefficient dS_{yr0}/dy was discontinuous in both positions and then power flows from the center line of the pattern interval parallel to the x-axis to each pattern edge of the pattern conductors facing each other as shown in the Fig. 11(a). Furthermore, the sign of S_{zr0} in both positions 11 and 12 was negative and power flows toward the back reflector. Therefore, most of the power flows from the pattern edge of the pattern conductor into the polymer layer between the pattern conductor and the back reflector. It is revealed that the pattern interval between the pattern conductors parallel to the x-axis plays an important role in the input and output of Poynting vectors.

Subsequently, with the non-matching condition of $W = 1$ mm shown in Fig. 7(a), the normalized
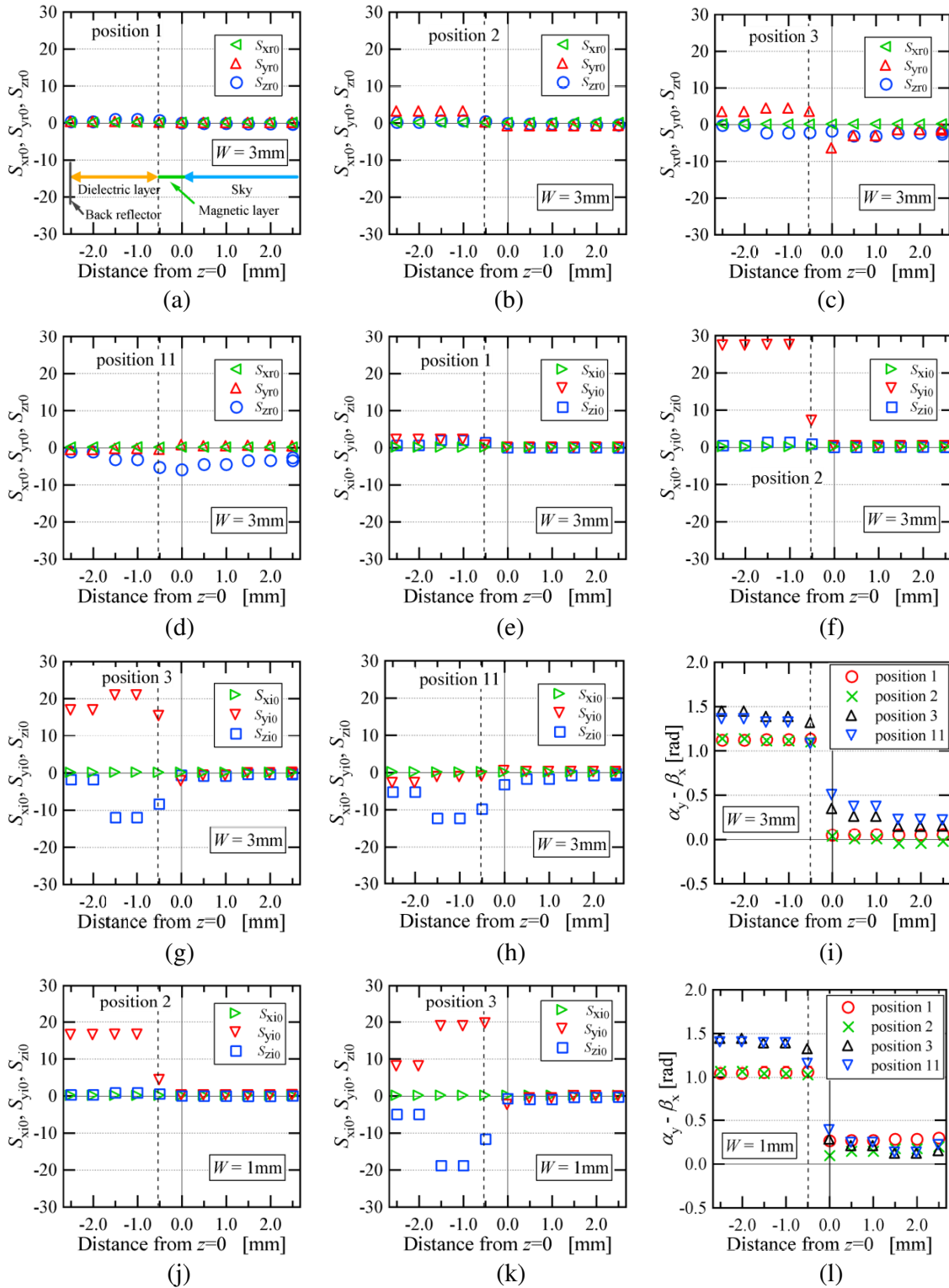
Figure 10. Normalized Poynting vectors for $W = 3\,\text{mm}$ in the positions (a), (e) 1, (b), (f) 2, (c), (g) 3 and, (d), (h) 11, and for $W = 1\,\text{mm}$ in the positions (j) 1, (k) 3, and phase angle difference $\alpha_y - \beta_x$ in each position for (i) $W = 3\,\text{mm}$ and for (l) $W = 1\,\text{mm}$ around the boundary between polymer layer and sky. (a), (b), (c), (d) real parts, (e), (f), (g), (h), (j), (k) imaginary parts.
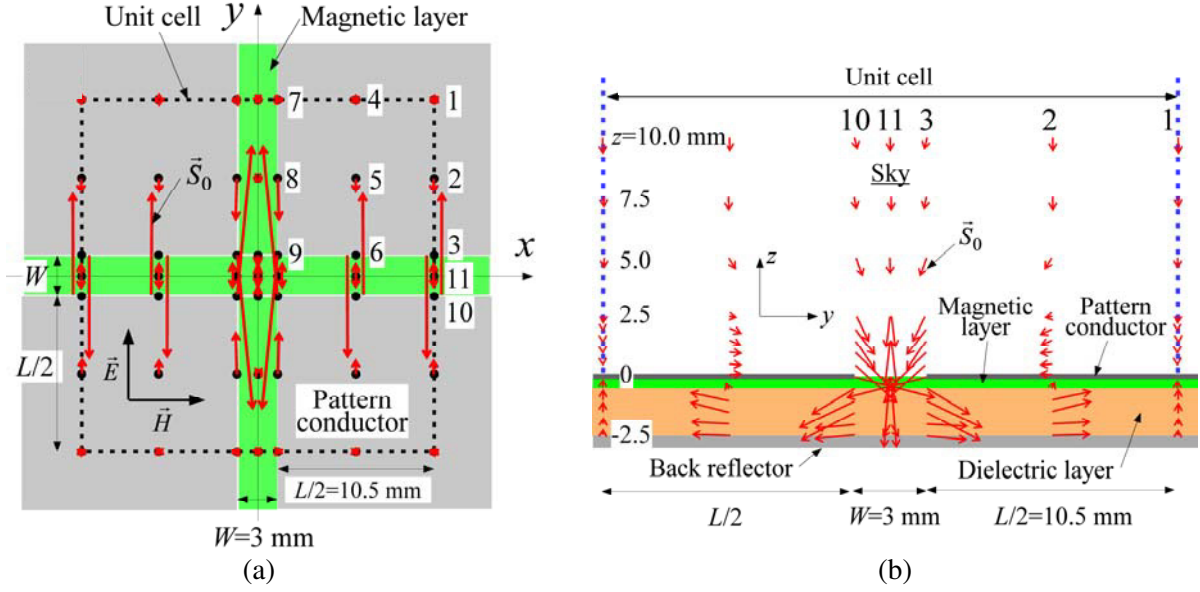
Figure 11. Schematic drawing of normalized Poynting vectors for $W = 3\,\text{mm}$ in unit cell on the x-y plane at $z = 0\,\text{mm}$ and on the y-z plane between $z = -2.5$ and $10.0\,\text{mm}$ in positions of 1, 2, 3, 11, 10 shown in Fig. 2(a) and the related positions.

Poynting vector components were calculated in all black points shown in Fig. 2(a), and some of those real and imaginary parts in the sky are shown in Fig. 9. When electromagnetic waves are irradiated on the pattern absorber, power is reflected in the horizontal direction similar to the matching condition of $W = 3\,\text{mm}$, and reflected waves due to mismatching are noticeable. S_{zr0} in all the positions became constant at $z \geq \sim 25\,\text{mm}$ in the sky. S_{zi0} was not 0 and oscillated with a wavelength of one-half of the spatial wavelength. The amplitude of oscillation was almost the same in all the positions. The ratio of the amplitude of S_{zi0} to the perfect reflection shown in Fig. 3(a) was ~ 0.201 and then the value of $20\log_{10}(0.201)$ was $\sim -14\,\text{dB}$. This value agreed well with the return loss value of $14.02\,\text{dB}$ for $W = 1\,\text{mm}$ shown in Table 2. Similar results were obtained for other W values. Therefore, S_{zi0} indicated the same standing wave behavior for the electric and magnetic field and as a result, the return loss can be calculated not only from S_{zr0} but S_{zi0}. S_{zr0} for $W = 1\,\text{mm}$ flowing toward the back of the polymer layer from the entrance of the pattern interval was larger than that for $W = 3\,\text{mm}$ as shown in Figs. 8(b) and (k) and Figs. 9(b) and (d), though the pattern interval was narrower than that for $W = 3\,\text{mm}$.

Particularly noteworthy is that although the reflection behavior in the vicinity of absorbers with different pattern interval W is different in any position, homogenization of the reflected waves occurs in the sky for $z > \sim 25\,\text{mm}$. It is suggested that evanescent modes included in the reflected waves are attenuated in the sky for $z > \sim 25\,\text{mm}$ and the homogeneous reflection behavior remains there.

The real parts S_{xr0}, S_{yr0}, and S_{zr0} of the Poynting vectors represent real power flows. The electromagnetic wave absorber is the medium in which this real power is converted into heat. On the other hand, the imaginary parts S_{xi0}, S_{yi0}, and S_{zi0} of the Poynting vectors represent reactive power, and are not converted into heat. However, both the real and imaginary parts are closely related. Thus, the wave attenuation due to wave interference is considered to be related to this imaginary power, and is an effective way to discuss the absorption characteristics of the electromagnetic wave absorber, although it is not physical.

3.3. Power Flow in Pattern Absorber

Figure 10 shows the behavior of the real and imaginary parts of the normalized Poynting vector $\vec{S}_0$ inside the polymer layer and in the sky, where are in the vicinity of the incident face in each position shown in

Fig. 2(a) for $W = 3$ and $1\,\text{mm}$ as examples. For $W = 3\,\text{mm}$, both the real and imaginary parts became almost zero inside and outside the polymer layer in position 1 according to the boundary condition as shown in Figs. 10(a) and (e). The real power (the real part of $\vec{S}_0$) mainly flowed in the y direction near the pattern conductor layer. It flows in the y-axis negative direction for the sky side and on the other hand in the y-axis positive direction for the polymer layer side in positions 2 and 3 (pattern edge), as shown in Figs. 10(b) and (c). Therefore, it is revealed that the real power flows into the resonator from the sky through the pattern interval. The reactive power (the imaginary part of $\vec{S}_0$) also mainly flowed in the y direction near the pattern conductor layer. A large reactive power flows into the resonator, as shown in Figs. 10(f), and (g). The magnitude becomes the largest inside the polymer layer in position 2, as shown in Fig. 10(f). This indicates that the reactive power is accumulated because the pattern conductor and the back reflector form a resonator with loss function. Because the phase angle difference $\alpha_y - \beta_x$ is close to $\pi/2\,\text{rad}$ in the polymer layer, the reactive power flow in the z direction is superior in the inside of polymer layer. The same tendency was also seen for $W = 1\,\text{mm}$. Then, what is the cause of the difference in the absorption characteristic for both $W = 1$ and $3\,\text{mm}$? Figs. 10(f) and (j) show the reactive power flow in position 2 for $W = 3$ and $1\,\text{mm}$, respectively. The magnitude of S_{yi0} for $W = 3\,\text{mm}$ is about twice as large as that for $W = 1\,\text{mm}$. This indicates that the twice as much power of an incidence wave is absorbed for $W = 3\,\text{mm}$ compared with $W = 1\,\text{mm}$ because about twice as much power flows in through the pattern interval and about twice as much power is accumulated in the resonator for $W = 3\,\text{mm}$ due to the larger area of the pattern interval as compared with $W = 1\,\text{mm}$.

In order to visualize what is described above, the real power flow is shown in a schematic drawing, Fig. 11. The real power flow on the x-y plane at $z = 0\,\text{mm}$ in each position for $W = 3\,\text{mm}$ is shown in Fig. 11(a) and that on the y-z plane in the height range of $z = -2.5\,\text{mm}$ to $+10\,\text{mm}$ at $x = 12\,\text{mm}$, which includes the positions 1, 2, 3, and 11, is shown in Fig. 11(b). It is revealed clearly that the real power of the electromagnetic wave, which is incident vertically to the pattern conductor, flows horizontally along the pattern conductor surface toward the pattern interval, and flows into the resonator.

Through the use of the Poynting vector related to anisotropy, it is found that the initial electromagnetic wave power incident on the resonant pattern conductor (the conductor antenna part at the upper end of the resonator) partially flows horizontally on/above the pattern conductor parallel to the electric field of the electromagnetic wave. The behavior of the Poynting vector confirms that the power is accumulated inside the pattern resonator and is finally converted into heat in the matching state.

4. CONCLUSIONS

 (i) The flow in each direction of the electromagnetic wave power in/around the pattern absorber could be evaluated using the Poynting vector.

 (ii) The results showed that an electromagnetic wave vertically incident on the pattern conductor of the pattern absorber was partially converted to a horizontal power flow, moved around the pattern conductor in a half circumference in the vertical direction, and entered inside the pattern absorber.

(iii) It is possible to reduce the thickness of the electromagnetic wave absorber in the vertical direction by securing the distance and volume of power dissipation inside the pattern absorber from the flow-path of the electromagnetic power.

(iv) The reflected waves became homogeneous in any points in the sky at a certain distance from the pattern conductor surface due to the voluntary power distribution effect.

 (v) Based on the principle of electromagnetic wave absorption, the real electromagnetic wave power flows horizontally along the surface of the pattern conductor after the incident wave enters the pattern absorber and the power flows merge as a downward flow together with opposite direction flow originated from adjacent patterns, and enters from the pattern interval. Then the main power is accumulated inside the pattern conductor. Absorption is caused by heat loss without a disappearance of the interference, which does not conform to the energy conservation law.

REFERENCES

1. Naito, Y. and K. Suetake, "Application of ferrite to electromagnetic wave absorber and its characteristics," *IEEE Trans. Microwave Theory and Technique*, Vol. 19, 65–72, 1971.

2. Lim, K. M., K. A. Lee, M. C. Kim, and C. G. Park, "Complex permeability and electromagnetic wave absorption properties of amorphous alloy-epoxy composites," *J. Non-Crystalline Solids Soc.*, Vol. 351, 75–83, 2005.

3. Sakai, K., Y. Wada, and S. Yoshikado, "Composite electromagnetic wave absorber made of permalloy or sendust and effect of sendust particle size on absorption characteristics," *PIERS Online*, Vol. 4, 846–853, 2008.

4. Wada, Y., N. Asano, K. Sakai, and S. Yoshikado, "Preparation and evaluation of composite electromagnetic wave absorbers made of fine aluminum particles dispersed in polystyrene resin by controlling permeability," *PIERS Online*, Vol. 4, 838–845, 2008.

5. Sakai, K. and S. Yoshikado, "Effect of particle shape on absorption characteristics of composite electromagnetic wave absorber made of sendust particles dispersed in polystyrene resin," *ICC3 IOP Conf. Ser.: Mater. Sci. Eng.*, Vol. 18, 092019, 2011.

6. Yoshida, T., Y. Agari, and S. Yoshikado, "Evaluation of absorbing characteristics and thermal contact resistance of electromagnetic wave absorbing composite rubber," *IEEJ Trans. FM*, Vol. 132, 180–186, 2012 (in Japanese).

7. Amano, M. and Y. Kotsuka, "A novel microwave absorber with surface-printed conductive line patterns," *IEEE MTT-S Digest*, 1193–1196, 2002.

8. Yoshida, T., M. Matsushita, T. Kubota, and S. Yoshikado, "Fabrication and evaluation of electromagnetic wave absorbers using frequency selective surface," *2016 Progress In Electromagnetic Research Symposium (PIERS)*, 1138–1144, IEEE Conference Publications, Shanghai, China, Aug. 8–11, 2016.

9. Rafael, P. and P. M. David, "A frequency-selective surface using aperture-coupled microstrip patches," *IEEE Trans. Antenna and Propagation*, Vol. 39, 1763–1769, 1991.

10. Nakajima, M., *The Microwave Engineering*, Morikita Publishing Co., Ltd, 36–37, 1975 (in Japanese).

11. Collin, R. E., *Foundation for Microwave Engineering*, McGraw-Hill, Inc., 1966.

12. Das, A., *Lectures on Electromagnetism*, 2nd Edition, World Scientific, 2013.

13. Christopoulos, C., *The Transmission-Line Modeling Method: TLM*, Wiley-IEEE Press, 1995.

14. Zhou, Y. J., X. Y. Zhou, T. J. Cui, R. Qiang, and J. Chen, "Efficient simulations of periodic structures with oblique incidence using direct spectral FDTD method," *Progress In Electromagnetic Research M*, Vol. 17, 101–111, 2011.

15. Belkhir, A. and F. I. Baida, "Three-dimensional finite-difference time-domain algorithm for oblique incidence with adaptation of perfectly matched layers and nonuniform meshing: Application to the study of a radar dome," *Phys. Rev. E*, Vol. 77, 056701-1–056701-10, 2008.

16. Johar, F. M., S. N. Salleh, F. A. Azmin, B. H. Ahmad, and M. Md. Shukor, "A review of method in FDTD for the analysis of oblique incident plane wave on periodic structures," *International Journal of Engineering and Technlogy (IJET)*, Vol. 5, 3900–3906, 2011.